Droplet spreading on a two-dimensional wicking surface

Chang Quan Lai,[1,*] Trong Thi Mai,[2,*] H. Zheng,[2] P. S. Lee,[3] K. C. Leong,[4] Chengkuo Lee,[2] and W. K. Choi[1,2,†]

[1]*Advanced Materials for Micro- and Nano-Systems Programme, Singapore-MIT Alliance, Singapore 117576*

[2]*Department of Electrical and Computer Engineering, National University of Singapore, Singapore 117576*

[3]*Department of Mechanical Engineering, National University of Singapore, Singapore 117576*

[4]*GLOBALFOUNDRIES Singapore Pte. Ltd, Singapore 738406*

The dynamics of droplet spreading on two-dimensional wicking surfaces were studied using square arrays of Si nanopillars. It was observed that the wicking film always precedes the droplet edge during the spreading process causing the droplet to effectively spread on a Cassie-Baxter surface composed of solid and liquid phases. Unlike the continual spreading of the wicking film, however, the droplet will eventually reach a shape where further spreading becomes energetically unfavorable. In addition, we found that the displacement-time relationship for droplet spreading follows a power law that is different from that of the wicking film. A quantitative model was put forth to derive this displacement-time relationship and predict the contact angle at which the droplet will stop spreading. The predictions of our model were validated with experimental data and results published in the literature.

　　　　　　　　PACS number(s): 68.08.Bc

I. INTRODUCTION

Two-dimensional (2D) wicking is a relatively new area of interest in wetting research, properly characterized and described only a decade ago by the seminal work of Bico *et al.* [1]. In that study, it was shown that when a liquid droplet is deposited on a hydrophilic solid surface that is sufficiently rough, it becomes energetically favorable for a thin film of liquid to extend from the base of the droplet and imbibe the surrounding roughness of the surface. Because it can be considered as an intermediate between spreading and wicking, the phenomenon is also known as hemiwicking [2].

The characteristics of the wicking liquid film has been extensively studied in recent years, giving rise to a substantial amount of literature covering the kinetics and thermodynamics of the subject. Extrand *et al.* [3], for instance, investigated the maximum spreading distance of oil droplets on a 2D wicking superoleophilic surface consisting of regular arrays of square pillars while Hay *et al.* [4], using a hydraulic diameter approximation, examined the resistance to the wicking flow due to the presence of microstructures on the surface. We have also conducted studies on the dynamics of 2D wicking recently, revealing that viscous dissipation [5] and form drag [6] caused by surface asperities are important factors in influencing the rate of imbibition by the wicking film.

In contrast, the spreading dynamics of the droplet, from which the wicking film is spawned, has received relatively less attention, although much work has been done to elucidate the spreading of droplets on flat solid surfaces [7–10], flat liquid surfaces [11], rough surfaces [12–17] and flat surfaces of composite chemistry [17]. McHale *et al.* [17], in particular, have derived the displacement-time relationships for droplet spreading on flat homogeneous surfaces, flat heterogeneous surfaces, and rough surfaces using hydrodynamic equations and dimensional analysis, but emphasized that their results are only valid when the effects of 2D wicking are excluded

from consideration. Clearly, a systematic study on the factors influencing droplet spreading on a 2D wicking surface is still lacking in the literature and this forms the objective of our present paper.

II. EXPERIMENTAL PROCEDURE

Two-dimensional wicking surfaces were produced by fabricating square arrays of nanopillars on 1cm × 1cm *p*-type (100) Si substrates using the laser interference lithography (LIL) with the Llyod's mirror setup and the metal assisted chemical etching (MACE) of silicon. The details of this fabrication process can be found in our earlier work [5,6]. Briefly, the LIL system was first used to expose 400 nm of spin-coated photoresist (Ultra-i-123) on a Si substrate twice, with each exposure at right angles to one another. After development with a commercial developer Microposit MF CD-26, photoresist dots will be left on the Si surface. Oxygen plasma processing was then employed to remove residual photoresist between the photoresist dots. To perform the MACE process, 30 nm of Au was deposited onto the surface using a thermal evaporator. Next, the removal of the photoresist was achieved by using acetone and ultrasonication, leaving behind an Au mesh with a square array of holes. Placing the samples into a bath containing 0.44 M of H_2O_2 and 4.6 M of HF will then cause preferential etching of Si under the Au mesh of holes, thus leaving behind Si nanopillars [18]. The height of the nanopillars can be controlled by etching duration. Lastly, the Au mesh was removed with a commercial Au etchant. An example of the fabricated Si nanopillars is shown in Fig. 1(a). Important geometrical parameters of the Si nanopillars and properties of deionized water used in this study can be found in Supplemental Material [19].

To examine the droplet-spreading behavior, the samples were placed horizontally on a microbalance shown in Fig. 1(b). The purpose of the microbalance was to measure the exact amount of liquid that was deposited quasistatically (∼1 mm/s) onto the center of the samples by means of a micropipette. Approximately 1 μl of deionized water was used for each experiment. The entire droplet spreading and 2D wicking

---

*These authors contributed equally to this work.

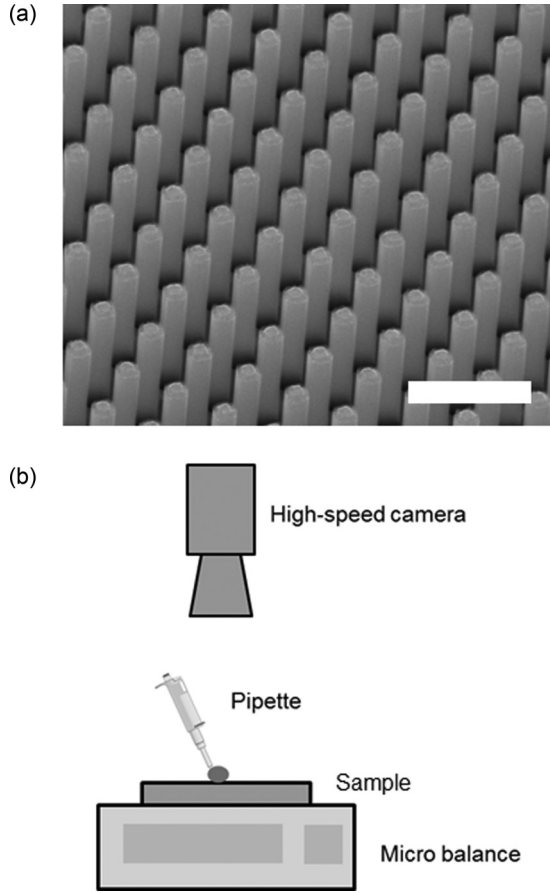†Corresponding author: elechoi@nus.edu.sg

(a)

(b)

FIG. 1. (a) SEM picture of Si nanopillars. Scale bar represents 2 μm. (b) Schematic diagram of setup employed to track droplet spreading over time.

process, which occurred simultaneously, was recorded by a high-speed camera (Photron Fastcam SA5) at 250 frames per second. Measurements of a, the distance from the center of the droplet to its edge or the wicking front, with respect to time, t, were then carried out on the captured video using the embedded software, Photron FASTCAM Viewer.

III. RESULTS AND DISCUSSION

A typical result of our experiments is presented in Fig. 2. When a droplet contacts and spreads on the Si surface, the droplet edge and the wicking front are initially almost indistinguishable. Approximately 10 ms after deposit of the droplet, however, a disparity in the kinematics of the two entities begins to set in, causing them to increasingly separate from each other over time [Fig. 2(a)]. In this time period ($t >$ 10 ms), the edge of the wicking film was found to always be ahead of the edge of the droplet [Fig. 2(b)]. In addition, it can also be seen that the droplet stops spreading after it reaches a maximum distance, a, while no such limit seems to exist for the spreading of the wicking film. This observation is also supported in other reports [1,5,6]. Lastly, it was noted that while the wicking film spreads in accordance to the proven diffusive relationship, $a \propto t^{1/2}$ [1,5,6], which arises out of a balance between the capillary force and the viscous dissipative force, the spreading of the droplet appears to follow a different

power law, as the droplet edge decelerated much more rapidly after the initial stages.

It is known that when a droplet first contacts a surface, the earliest stage of droplet spreading ($t <$ 10 ms for our study) is dominated by the balance between Laplace pressure and the inertia of the droplet, which leads to a characteristic $a \propto t^{\alpha}$ relationship, where α generally ranges from 0.3–0.5, depending on the wettability of the surface [20,21]. We shall term this stage the capillary-inertia regime since Laplace pressure arises from surface tension. Our results show that both the droplet and the wicking film were influenced by this balance of capillary and inertia forces to similar extents in the early stages. This is reasonable since the curvature and mass of the droplet are the most crucial factors affecting the dynamics of spreading in this regime [20,21] instead of the substrate surface properties, which give rise to 2D wicking.

In the later stages ($t >$ 10 ms), droplet spreading becomes determined mainly by the balance of capillary energy and viscous dissipation (i.e., the capillary-viscous regime), which explains the $a \propto t^{1/2}$ relationship for the wicking front [2,5,6,22]. This latter regime shall be the focus of this study, where the dynamics of spreading are expected to be more affected by the presence of nanostructures on the surface and because of practical limitations in our experimental setup (at 250 fps, we can only obtain two data points for $t <$ 10 ms).

To quantitatively understand the relationship between a and t for droplet spreading, we begin by considering a model such as that illustrated in Fig. 3, based on our observations presented above. In this model, the wicking film, which precedes the droplet edge, has filled up the space between the nanopillars, leaving only the top of the nanopillars dry. Therefore, the droplet, which assumes the shape of a spherical cap, spreads on a flat surface made up of ϕ_s fraction of solid and (1-ϕ_s) fraction of liquid. This sort of composite surface is commonly referred to as a Cassie-Baxter surface [17,23]. At the edge where it meets the Cassie-Baxter surface, the droplet deforms from its spherical cap shape to form a microscopic liquid wedge and precursor film [24], the profiles of which we will model here simply as a flat film with a thickness of δ (Fig. 3).

For simplicity, we will assume that the spreading of the droplet across the composite flat surface can effectively be described with Poiseuille's flow [1],

$$U = \frac{\delta^2 \Delta P}{3\mu a},\tag{1}$$

where U is the velocity of the edge of the droplet, μ is the viscosity of the liquid and ΔP refers to the capillary pressure driving the droplet spreading.

Since it has been proven that the wicking film essentially advances using only the capillary energy it gains from wetting the nanopillars as it spreads, it can be construed that, likewise, droplet spreading is driven only by the capillary energy the droplet gains as it wets the Cassie-Baxter surface. In other words, the wicking film and the droplet can be considered as independent systems. ΔP can therefore be expressed as

$$\Delta P = -\frac{1}{2\pi a \delta} \frac{dE}{da}$$
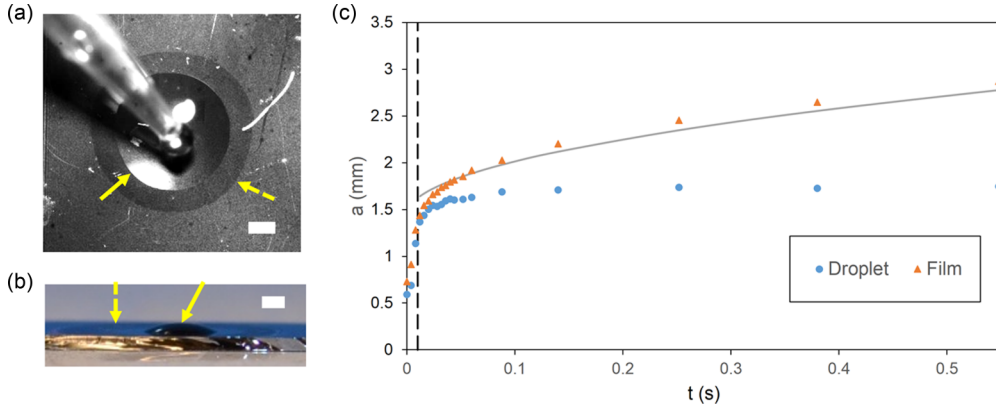$$= \frac{\gamma}{\delta} \left[\frac{2H^2}{a^2 + H^2} - \varphi_s (1 - \cos\theta) \right],\tag{2}$$

FIG. 2. (Color online) (a) Top view and (b) side view a droplet spreading on a 2D wicking surface. The solid arrow points to the droplet while the dashed arrow points to the wicking film. Scale bar represents 1 mm. (c) Representative plot of a vs t for the droplet edge and wicking front. The vertical dashed line marks $t = 10$ ms and the green curve represents the function $a \propto t^{1/2}$.

where γ is the surface tension of the liquid, H refers to the height of the droplet, and θ is the contact angle the liquid makes with a flat surface of the substrate material. Note that for deionized water on Si, $\theta = 56.3°$. dE is the capillary energy gained by the system when the droplet spreads an infinitesimal distance of $da \cdot \frac{dE}{da}$ can be found by the addition of two components: the increase in surface energy due to the flattening of the curved spherical cap surface and the decrease in surface energy due to the obliteration of ϕ_s fraction of solid surface and $(1-\phi_s)$ fraction of liquid surface when the droplet spreads over a distance of da on the Cassie-Baxter surface. Substituting the addition of these two terms for $\frac{dE}{da}$ then leads to the expression on the right. The detailed derivation of Eq. (2) can be found in Supplemental Material [19].

With Eq. (2), we can then rewrite Eq. (1) as

$$U = \frac{\delta\gamma}{3\mu a}\left[\frac{2H^2}{a^2 + H^2} - \varphi_s(1 - \cos\theta)\right] \tag{3}$$

From Eq. (3), it can be observed that the droplet will stop spreading ($U = 0$) when

$$\frac{a}{H} = \sqrt{\frac{2}{\varphi_s(1 - \cos\theta)} - 1}. \tag{4}$$

Using geometry and small-angle approximation [19], the apparent contact angle $\theta*$ at which the droplet will stop

spreading can be found to be

$$\theta* = \frac{2}{\sqrt{\frac{2}{\varphi_s(1-\cos\theta)} - 1}}. \tag{5}$$

Note that the contact angle of the droplet will not stay as $\theta*$ but will, instead, diminish over time as the wicking film continues to spread and drain the droplet. However, for the time period where the droplet generally stops spreading ($t \leq 0.3$s), we have verified that the volume of liquid taken up by the wicking film is negligible and can be ignored in the calculations.

In Fig. 4, we compare $\theta*$ predicted by Eq. (5), which was derived through a kinetics approach, with that predicted by Bico _et al_. [1,2] using a thermodynamics approach,

$$\cos\theta* = 1 - \varphi_s(1 - \cos\theta). \tag{6}$$

It can be observed that there is little difference between the results of Eqs. (5) and (6) except at large value of $\theta*$ (i.e., small $\cos\theta*$) where our small-angle approximation of $\theta*$ breaks down. This is not entirely unexpected as both the kinetic and thermodynamic approaches share the common assumption that capillary energy gained by the droplet during spreading is the main driving force for wetting. As can be seen from Fig. 4, our experimental results support this assumption along with results from other studies [1,2]. The good agreement of Eq. (5),
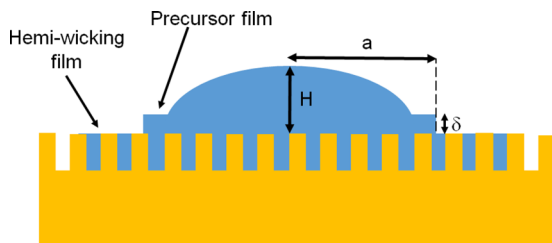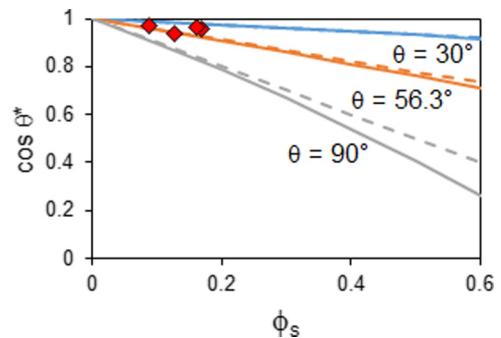

FIG. 3. (Color online) Schematic diagram showing a droplet spreading on a wicking film imbibed between the nanopillars. The sides, but not the top, of the nanopillars are wetted by the wicking film. The size of the precursor film has been exaggerated for clarity.

FIG. 4. (Color online) Plots of Eq. (5) (solid lines) and Eq. (6) (dashed lines) for various values of θ. Experimental data (for $\theta = 56.3°$) are plotted as diamonds.

Eq. (6), and experimental data serves to validate our analysis up to this point.

Going further, we noted from our experimental data that for the capillary-viscous regime of droplet spreading we are interested in, a/H is much greater than 1. Droplet shapes with $a/H \leq 1$ are mainly found in the preceding capillary-inertia regime. Hence, from the conservation of volume, $H \approx \frac{2V}{\pi a^2}$, where V refers to the volume of the droplet deposited. As such, Eq. (3) can be rewritten as

$$\frac{\pi^2 a^7}{8V^2 \left[1 - \frac{\pi^2 \varphi_s (1 - \cos\theta)}{8V^2} a^6\right]} \frac{da}{dt} = \frac{\delta\gamma}{3\mu}. \tag{7}$$

Note that we have substituted U with da/dt in the above equation. The integration of Eq. (7) cannot be performed easily and requires some simplification. Therefore, we make the following approximation using binomial expansion,

$$\left[1 - \frac{\pi^2 \varphi_s (1 - \cos\theta)}{8V^2} a^6\right]^{-1}$$
$$\approx 1 + \frac{\pi^2 \varphi_s (1 - \cos\theta)}{8V^2} a^6 + \left[\frac{\pi^2 \varphi_s (1 - \cos\theta)}{8V^2}\right]^2 a^{12}, \tag{8}$$

noting from Eq. (7) that da/dt (i.e., U) will only have a positive value when $\frac{\pi^2 \varphi_s (1 - \cos\theta)}{8V^2} a^6 < 1$. Combining Eqs. (7) and (8) and integrating [19], we finally arrive at

$$t \approx \frac{3\mu}{\delta\gamma} \left[\frac{\pi^2}{64V^2} a^8 + \frac{\pi^4 \varphi_s (1 - \cos\theta)}{896V^4} a^{14} \right.$$
$$\left. + \frac{\pi^6 \varphi_s^2 (1 - \cos\theta)^2}{10240V^6} a^{20}\right]. \tag{9}$$

Figure 5(a) shows a typical plot of t versus X where X represents $\frac{\pi^2}{64V^2} a^8 + \frac{\pi^4 \varphi_s (1 - \cos\theta)}{896V^4} a^{14} + \frac{\pi^6 \varphi_s^2 (1 - \cos\theta)^2}{10240V^6} a^{20}$. It can be seen from the plot that the relationship between t and X is indeed linear, as predicted by Eq. (9). It can also be observed that there is a small but finite value for the y intercept, which is likely caused by the extended effects of the previous stage of droplet spreading (i.e., in the capillary-inertia regime).

To further verify our analysis, we obtained the gradients of t versus X plots from five samples, each having a different surface roughness, r. This surface roughness can be varied by changing the height of the nanopillars and its quantitative value is given by the ratio of the actual solid surface area to the projected area [1,5]. As can be seen from Fig. 5(b), the value of the gradient and by implication, the droplet-spreading behavior, is not dependent on r.

This result is in line with our analysis, which is based on the assumption that regardless of the height of the nanopillars, they would be immersed in the wicking film for the full length of their height. Therefore, the droplet will spread on the same Cassie-Baxter surface (if ϕ_s and θ are the same) even if the surface roughness of the samples is different, leading to the observed invariance of droplet-spreading behavior with respect to r. This is succinctly described by Eq. (9), which shows that the relationship between a and t will only depend on γ, μ, δ, ϕs, V, and θ but not r.

In addition, from Eq. (9) and the average value of the gradients in Fig. 5(b), we find that $\delta = 12\,\mu$m. This calculated size
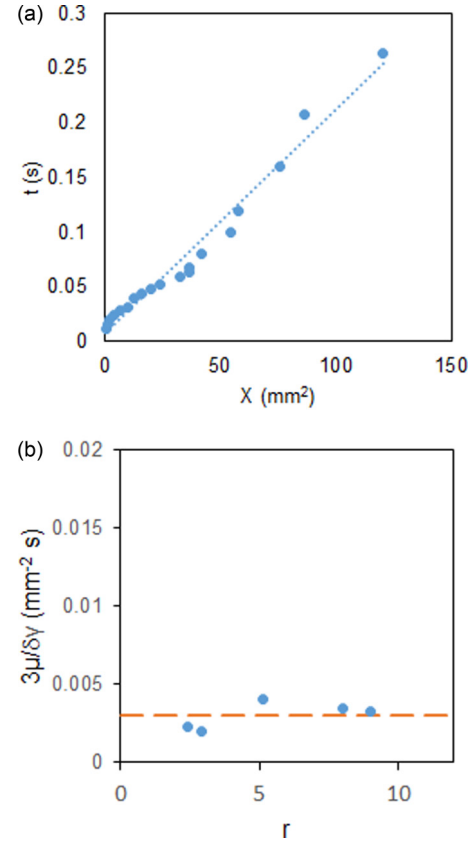

FIG. 5. (Color online) (a) A representative plot of t versus X. (b) Plot of gradient, $3\mu/\delta\gamma$, versus r. Dashed line shows the average value of the data points.

of the precursor film corresponds very well with that observed in SEM pictures (10–20 μm) [25] and further validates our analysis. The fact that δ is a constant is not surprising given the fact that the droplet volume and surface on which it is spreading is similar (due to the Cassie-Baxter nature of the surface) across the samples. Substituting the value for δ back into Eq. (9) will then provide us with a complete description of the kinetics of droplet spreading on a 2D wicking surface. From Fig. 6, it can be seen that there is very good agreement between our experimental a versus t data and the relationship
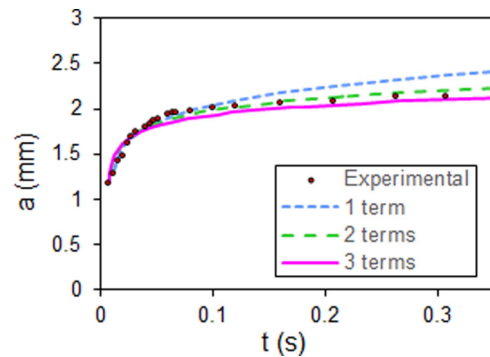

FIG. 6. (Color online) Plot of a vs t. The different lines show the binomial approximation in Eq. (9) carried out to different number of terms respectively.

described in Eq. (9), especially when the binomial expansion is carried out to more than one term.

There are a few interesting insights that can be learned from our study. For instance, the dynamics of droplet spreading on a 2D wicking surface is found to be much more affected by the properties of the liquid droplet than the solid surface it is spreading on. This is evident from the relative lack of dependence of Eq. (9) on ϕ_s $(1-\cos\theta)$ as compared to γ, μ, and V.

In fact, the coefficients in the second and third term in Eq. (9) are so small that the terms are only significant at large values of a (see Fig. 6). Therefore, in the early stages of wetting in the capillary-viscous regime where a is relatively small, the second and third term of Eq. (9) can be ignored so that

$$t \approx \frac{3\pi^2\mu}{64V^2\delta\gamma}a^8. \tag{10}$$

In other words, $a \propto t^{0.125}$. It is worth noting from Eq. (10) that in this early capillary-viscous regime, the droplet-spreading behavior is independent of the fraction and surface energy of the solid substrate, as characterized by ϕ_s and $\cos\theta$ respectively, suggesting that the same droplet-spreading dynamics can be expected to be observed on 2D wicking surfaces with different forms of nanostructures (e.g., irregular arrays) and hydrophilicity.

As a increases, the second and third terms of Eq. (9) become significant and add to the value of t so that for a given a, t is larger in Eq. (9) than in Eq. (10). Therefore, if Eq. (9) is fitted to the form of $a \propto t^n$, n would be smaller than 0.125.

This result agrees well with the results of McHale *et al.*'s [17] more stringent derivation for droplet spreading on a Cassie-Baxter surface, $a \propto t^{0.1}$. We note, however, that our approach offers a more complete description of the a-t relationship, thus allowing us to obtain more insights into the dynamics of droplet spreading on a 2D wicking surface.

IV. CONCLUSIONS

In conclusion, we have studied the dynamics of droplet spreading on a 2D wicking surface and found that the process is essentially equivalent to a droplet spreading on a Cassie-Baxter surface. This is due to the presence of a wicking film, which always precedes the droplet edge. As a result, the dynamics of droplet spreading was found to be invariant with respect to the surface roughness, depending mainly on the properties of the liquid droplet and to a smaller extent, on the density of the nanostructures and the hydrophilicity of the solid surface. These results are in line with expectations in the current literature and the insights derived in this study contribute to a better understanding of the fundamental process of droplet spreading.

[1] J. Bico, C. Tordeux, and D. Quéré, Eur. Phys. Lett. **55**, 214 (2001).

[2] J. Bico, U. Thiele, and D. Quéré, Colloids Surf. A **206**, 41 (2002).

[3] C. W. Extrand, S. I. Moon, P. Hall, and D. Schmidt, Langmuir **23**, 8882 (2007).

[4] K. M. Hay, M. I. Dragila, and J. Liburdy, J. Colloid Interface Sci. **325**, 472 (2008).

[5] T. T. Mai, C. Q. Lai, H. Zheng, K. Balasubramanian, K. C. Leong, P. S. Lee, C. Lee, and W. K. Choi, Langmuir **28**, 11465 (2012).

[6] C. Q. Lai, T. T. Mai, H. Zheng, P. S. Lee, K. C. Leong, C. Lee, and W. K. Choi, Appl. Phys. Lett. **102**, 053104 (2013).

[7] L. H. Tanner, J. Phys. D: Appl. Phys. **12**, 1473 (1979).

[8] J. A. Diez, R. Gratton, L. P. Thomas, and B. Marino, J. Colloid Interface Sci. **168**, 15 (1994).

[9] J.-D. Chen, J. Colloid Interface Sci. **122**, 60 (1988).

[10] D. Bonn, J. Eggers, J. Indekeu, J. Meunier, and E. Rolley, Rev. Mod. Phys. **81**, 739 (2009).

[11] S. L. Cormier, J. D. McGraw, T. Salez, E. Raphaël, and K. Dalnoki-Veress, Phys. Rev. Lett. **109**, 154501 (2012).

[12] N. Savva and S. Kalliadasis, Phys. Fluids **21**, 092102 (2009).

[13] N. Savva, S. Kalliadasis, and G. A. Pavliotis, Phys. Rev. Lett. **104**, 084501 (2010).

[14] N. Savva, G. A. Pavliotis, and S. Kalliadasis, J. Fluid Mech. **672**, 358 (2011).

[15] N. Savva, G. A. Pavliotis, and S. Kalliadasis, J. Fluid Mech. **672**, 384 (2011).

[16] C. Q. Lai, C. V. Thompson, and W. K. Choi, Langmuir **28**, 11048 (2012).

[17] G. McHale, M. I. Newton, and N. J. Shirtcliffe, J. Phys. Condens. Matter **21**, 464122 (2009).

[18] W. K. Choi, T. H. Liew, M. K. Dawood, H. I. Smith, C. V. Thompson, and M. H. Hong, Nano Lett. **8**, 3799 (2008).

[19] See Supplemental Material at http://link.aps.org/supplemental/10.1103/PhysRevE.88.062406 for details on the dimensions of the nanostructures and the derivations for various equations used in this study.

[20] A.-L. Biance, C. Clanet, and D. Quéré, Phys. Rev. E **69**, 016301 (2004).

[21] J. C. Bird, S. Mandre, and H. A. Stone, Phys. Rev. Lett. **100**, 234501 (2008).

[22] C. Ishino, M. Reyssat, E. Reyssat, K. Okumura, and D. Quéré, Eur. Phys. Lett. **79** 56005 (2007).

[23] A. B. D. Cassie and S. Baxter, Trans. Faraday Soc. **40**, 546 (1944).

[24] P. G. de Gennes, Rev. Mod. Phys. **57**, 827 (1985).

[25] W. Choi, A. Tuteja, J. M. Mabry, R. E. Cohen, and G. H. McKinley, J. Colloid Interface Sci. **339**, 208 (2009).